

# Continuum model for the terahertz dielectric response of glasses

Tatsuya Mori,<sup>1,\*</sup> Hideyuki Mizuno,<sup>2</sup> Dan Kyotani,<sup>1</sup> Soo Han Oh,<sup>1</sup> Yuzuki Motokawa,<sup>1</sup> Yasuhiro Fujii,<sup>3,4</sup> Akitoshi Koreeda,<sup>5</sup> Shinji Kohara,<sup>6</sup> and Seiji Kojima<sup>1</sup>

<sup>1</sup>*Department of Materials Science, University of Tsukuba,  
1-1-1 Tennodai, Tsukuba, Ibaraki 305-8573, Japan*

<sup>2</sup>*Graduate School of Arts and Sciences, The University of Tokyo,  
3-8-1 Komaba, Meguro-ku, Tokyo 153-8902, Japan*

<sup>3</sup>*Institute for Open and Transdisciplinary Research Initiatives,  
Osaka University, 2-1 Yamada-oka, Suita, Osaka 565-0871, Japan*

<sup>4</sup>*Research Organization of Science and Technology, Ritsumeikan University,  
1-1-1 Noji-higashi, Kusatsu, Shiga 525-8577, Japan*

<sup>5</sup>*Department of Physical Sciences, Ritsumeikan University,  
1-1-1 Noji-higashi, Kusatsu, Shiga 525-8577, Japan*

<sup>6</sup>*Center for Basic Research on Materials, National Institute for Materials  
Science (NIMS), 1-2-1 Sengen, Tsukuba, Ibaraki 305-0044, Japan*

Boson peak dynamics in glasses produce a robust crossover in the terahertz (THz) dielectric response that standard Debye or Lorentz models do not capture. We develop a continuum description of this THz response, coupling an infrared-effective charge fluctuation spectrum to a frequency-dependent shear modulus, and apply it to glycerol glass. The model reproduces the measured complex dielectric function and the nearly linear infrared light-vibration coupling around the boson peak, and highlights the dominant role of transverse shear dynamics.

In disordered solids, a universal excess of vibrational modes appears in the terahertz (THz) range—the boson peak (BP)—which is observed as a peak in the reduced vibrational density of states (VDOS)  $g(\omega)/\omega^{D-1}$  (where  $D$  is the spatial dimension) relative to the Debye level [1, 2]. Despite decades of work, the microscopic origin of the BP remains an open problem that continues to stimulate experiments [3–12], simulations [13–19], and theory [20–27]. The BP is tied to several hallmark anomalies of glasses: unusually low thermal conductivity [3], nanoscale plasticity [14], and a marked decrease in transmittance in the THz region above the BP frequency [11, 12]. Understanding the BP and its coupling to light is essential for fundamental physics and for predicting and controlling THz optical properties. In particular, emerging THz communication technologies demand window and substrate materials with low permittivity and low loss [28]. Motivated by these considerations, we focus on the dielectric response in the THz regime and develop a framework that connects the observed absorption to the underlying vibrational dynamics. Empirically, the THz dielectric response  $\varepsilon(\omega)$  in glasses shows a robust pattern that standard models fail to capture: below the BP frequency  $\omega_{\text{BP}}$  the response is resonance-like (Lorentz-oscillator-like), whereas above  $\omega_{\text{BP}}$  it becomes relaxational (Debye-like) [11, 12]. Neither standard relaxational dielectric functions—Debye and common empirical generalizations (e.g., the Havriliak–Negami form [29])—nor an over-damped Lorentz oscillator reproduces this crossover; a unified analytic form for  $\varepsilon(\omega)$  that captures this universal crossover has been lacking.

Several beyond-Debye/Lorentz approaches have been

pursued for the THz dielectric anomaly around the BP. Zacccone and co-workers formulated a phonon-polaritonic response by extending a Lorentz oscillator with a wavenumber-dependent damping  $\Gamma(k)$ , but the choice of  $\Gamma(k)$  limits transferability across different glasses [30]. A different route links dielectric relaxation to viscoelasticity: in the Gemant–DiMarzio–Bishop model the constant Debye viscosity is replaced by a frequency-dependent one, which can be expressed via a complex shear modulus [31, 32]. However, the model was devised for liquid-side relaxation and carries an explicit temperature dependence, making a direct application to low-temperature glass spectra nontrivial. Along this line, Zeitler *et al.* discussed the scaling  $g(\omega)/\omega^2 \propto \alpha(\omega)/\omega^3$  (with  $\alpha(\omega)$  the absorption coefficient) [33]; nevertheless, a unified, material-independent  $\varepsilon(\omega)$  capturing the BP crossover remains elusive.

Building on Maradudin’s linear-response theory for optical phonons in crystals [34] and decomposing the effective atomic-charge fluctuations into correlated (crystal-like) and uncorrelated (disorder-induced) parts, Taraskin derived the universal analytic form for the infrared (IR) light-vibration coupling coefficient  $C_{\text{IR}}(\omega) = \alpha(\omega)/g(\omega) = A + B\omega^2$ , which reproduces the IR absorption of silica and several other oxide glasses [35]. However, for glycerol the experimentally extracted  $C_{\text{IR}}(\omega)$  displays a pronounced linear dependence in the vicinity of the BP, clearly deviating from  $A + B\omega^2$  (see Fig. 2(b)). Similar linear trends have been reported for a broad range of amorphous materials, including hydrogen-bonded [11] and polymeric glasses [36], proteins [12], and even some inorganic glasses [37]. These observations call for a formulation that explains the linear  $C_{\text{IR}}(\omega)$  while remaining

consistent with the measured complex dielectric function  $\varepsilon(\omega)$  (both its real and imaginary parts,  $\varepsilon'(\omega)$  and  $\varepsilon''(\omega)$ ).

In this work, we introduce a continuum model that explicitly incorporates the IR-effective charge fluctuation spectrum  $\Delta q(k)$  and the effective complex shear modulus  $G(\omega)$ . With a low- $k$  form  $\Delta q(k) \approx q_0 + q_2 k^2$ , the model simultaneously reproduces  $\varepsilon'(\omega)$  and  $\varepsilon''(\omega)$  and accounts for the linear frequency dependence of  $C_{\text{IR}}(\omega)$  in the BP region, in quantitative agreement with experimental data. Moreover, by increasing the constant-to-quadratic ratio  $R \equiv q_0/(q_2 k_D^2)$  ( $k_D$  is the Debye wavenumber), the response continuously approaches a Taraskin-like form, so the present framework both explains the linear regime and contains the Taraskin expression as a limiting case.

We describe the THz dielectric response of a glassy solid using an isotropic viscoelastic continuum with bulk modulus  $K$ , complex shear modulus  $G(\omega)$ , and local IR-effective charge fluctuations  $\Delta q(\mathbf{r})$ . In the frequency domain, the displacement field  $\mathbf{u}(\mathbf{r}, \omega)$  driven by a spatially uniform THz electric field  $\mathbf{E}(\omega) = E(\omega) \hat{\mathbf{e}}$  obeys

$$\begin{aligned} -\rho\omega^2 \mathbf{u}(\mathbf{r}, \omega) = & \left( K + \frac{4}{3}G(\omega) \right) \nabla(\nabla \cdot \mathbf{u}(\mathbf{r}, \omega)) \\ & - G(\omega) \nabla \times (\nabla \times \mathbf{u}(\mathbf{r}, \omega)) \\ & + \Delta q(\mathbf{r}) \mathbf{E}(\omega). \end{aligned} \quad (1)$$

where  $\rho$  is the mass density. We expand the fields in plane waves and decompose each mode into the three acoustic branches  $\alpha = L, T_1, T_2$  with polarization vectors  $\hat{\mathbf{e}}_\alpha(\mathbf{k})$  ( $\hat{\mathbf{e}}_L = \mathbf{k}/|\mathbf{k}|$ ,  $\hat{\mathbf{e}}_{T_i} \cdot \mathbf{k} = 0$ ). The uniform field couples to branch  $\alpha$  through the scalar projection  $E_\alpha(\omega) = (\hat{\mathbf{e}} \cdot \hat{\mathbf{e}}_\alpha) E(\omega)$ . Fourier transforming Eq. (1) and projecting onto branch  $\alpha$  give the mode equation

$$(-\rho\omega^2 + C_\alpha(\omega)k^2)u_\alpha(\mathbf{k}, \omega) = \Delta q(\mathbf{k})E_\alpha(\omega), \quad (2)$$

with  $k = |\mathbf{k}|$ ,  $C_L(\omega) = M(\omega) = K + \frac{4}{3}G(\omega)$ , and  $C_{T_1}(\omega) = C_{T_2}(\omega) = G(\omega)$ . The macroscopic polarization component parallel to the field is  $P(\omega) = V^{-1} \int d^3r \Delta q(\mathbf{r}) \hat{\mathbf{e}} \cdot \mathbf{u}(\mathbf{r}, \omega)$ . Combining this definition with Eq. (2) and performing disorder and orientational averages (see Supplemental Material [38]) yields

$$\varepsilon(\omega) = \varepsilon_\infty + \frac{1}{\rho\varepsilon_0} \sum_\alpha \int_0^{k_D} \frac{\langle |\Delta q(k)|^2 \rangle_{\text{dis}} \gamma_\alpha 3k^2}{-\omega^2 + \tilde{C}_\alpha(\omega)k^2} \frac{dk}{k_D^3}, \quad (3)$$

where  $\tilde{C}_\alpha(\omega) = C_\alpha(\omega)/\rho$ ,  $\langle |\Delta q(k)|^2 \rangle_{\text{dis}}$  is the variance of the IR-effective charge fluctuations, and  $\gamma_\alpha = \langle (\hat{\mathbf{e}} \cdot \hat{\mathbf{e}}_\alpha)^2 \rangle_{\text{angles}}$  is the orientational coupling factor. In an isotropic three-dimensional elastic medium, the three acoustic polarizations form an orthonormal triad and are statistically equivalent, so that  $\gamma_L = \gamma_{T_1} = \gamma_{T_2} = 1/3$ . Grouping the two degenerate transverse branches and assuming that  $\langle |\Delta q(k)|^2 \rangle_{\text{dis}}$  is branch-independent, Eq. (3)

TABLE I. Model parameters for glycerol glass at 80 K used in Fig. 1.  $\rho$  is the mass density and  $K$  the bulk modulus [46];  $k_D$  is the Debye wavenumber, and  $\varepsilon_\infty$  the high-frequency dielectric constant.  $q_0$  and  $q_2$  specify the quadratic parameterization of the IR-effective charge spectrum  $\Delta q(k) = q_0 + q_2 k^2$ . The frequency-dependent shear modulus  $G(\omega)$  employed in the calculation is shown in Fig. S1.

	$\rho$ (g cm <sup>-3</sup> )	$k_D$ (Å <sup>-1</sup> )	$K$ (GPa)	$\varepsilon_\infty$	$q_0$ (C cm <sup>-3</sup> )	$q_2$ (C cm <sup>-3</sup> Å <sup>2</sup> )
Glycerol	1.26	1.90	10.58	2.765	0	$1.6 \times 10^{-3}$

reduces to

$$\begin{aligned} \varepsilon(\omega) = \varepsilon_\infty + & \frac{1}{\rho\varepsilon_0} \int_0^{k_D} \left[ \frac{2}{3} \frac{\langle |\Delta q(k)|^2 \rangle_{\text{dis}}}{-\omega^2 + \tilde{G}(\omega)k^2} \right. \\ & \left. + \frac{1}{3} \frac{\langle |\Delta q(k)|^2 \rangle_{\text{dis}}}{-\omega^2 + \tilde{M}(\omega)k^2} \right] \frac{3k^2}{k_D^3} dk. \end{aligned} \quad (4)$$

where  $\tilde{G}(\omega) = G(\omega)/\rho$  and  $\tilde{M}(\omega) = M(\omega)/\rho$ . Equation (4) is the expression used to analyze the THz dielectric response and the BP-related excess contribution. For quantitative comparison with experiment, the model inputs are  $\rho$ ,  $k_D$ ,  $G(\omega)$ ,  $K$ , and  $\Delta q(k)$ . For glycerol we use an effective shear modulus  $G(\omega)$  obtained from a heterogeneous-elasticity-theory coherent-potential-approximation (HET-CPA) analysis of the vibrational density of states  $g(\omega)$ , following our previous work [44], and parameterize the IR-effective charge spectrum by retaining the leading terms of a Maclaurin expansion,  $\Delta q(k) \approx q_0 + q_2 k^2$ . Because the dielectric spectra are insensitive to  $q_0$  within the experimental uncertainty, we fix  $q_0 = 0$ . The remaining parameter  $q_2$  is selected by a parameter scan to minimize the misfit between calculated and measured  $\varepsilon'(\omega)$  and  $\varepsilon''(\omega)$  (see Supplemental Material [38]). The parameters used in Fig. 1 are summarized in Table I.

The complex dielectric function  $\varepsilon(\omega)$  of glycerol glass was measured by terahertz time-domain spectroscopy (THz-TDS) [11, 12] using a commercial system (RT-10000, Tochigi Nikon Co.). The usable frequency range was approximately 0.2–2.5 THz. The THz beam path was enclosed in dry air, and the sample was mounted in a liquid-helium flow cryostat for temperature control between 14 and 295 K.

Glycerol ( $\geq 99.5\%$ , Sigma-Aldrich) was sealed in a liquid cell with a 0.2 mm optical thickness between two  $z$ -cut  $\alpha$ -quartz windows. The sample was vitrified *in situ* by cooling through the glass transition ( $T_g \simeq 190$  K [45]); the data analyzed correspond to the glassy state at 80 K after equilibration. Optical constants were extracted from a standard slab-transmission analysis to obtain the complex refractive index  $n(\omega)$ , and the complex dielectric function was then calculated via  $\varepsilon(\omega) = n^2(\omega)$ .

Figure 1 shows that our model simultaneously repro-

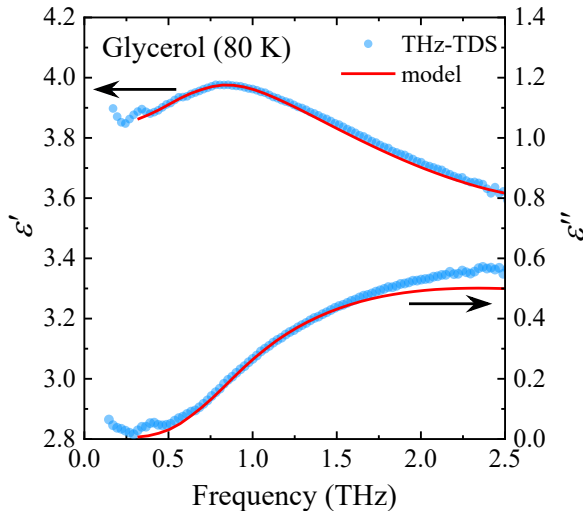


FIG. 1. Complex dielectric response of glycerol glass at 80 K. Symbols: THz-TDS measurements; solid curves: model. Plotted are  $\varepsilon'(\omega)$  and  $\varepsilon''(\omega)$  versus frequency (THz). The model reproduces the crossover from resonance-like behavior below  $\omega_{\text{BP}}$  to a broad Debye-like response above  $\omega_{\text{BP}}$ . The weak convex-upward feature in  $\varepsilon'(\omega)$  near  $\omega_{\text{BP}}$  is consistent with a shallow dip in  $G'(\omega)$ , i.e., a reduction of  $V_{\text{TA}}(\omega) = \sqrt{G'(\omega)/\rho}$  associated with the BP.

duces the measured real and imaginary parts,  $\varepsilon'(\omega)$  and  $\varepsilon''(\omega)$ , of glycerol glass across the THz range. Around the BP frequency  $\omega_{\text{BP}}$  the response crosses over from resonance-like behavior below  $\omega_{\text{BP}}$  to a broad, Debye-like lineshape above  $\omega_{\text{BP}}$ , in quantitative agreement with experiment. This agreement is naturally explained if optical attenuation is mediated by the effective complex shear modulus  $G(\omega)$ : Rayleigh-like scattering of long-wavelength acoustic modes prevails below  $\omega_{\text{BP}}$ , whereas above  $\omega_{\text{BP}}$  the dissipation associated with effective elastic heterogeneities is captured by a rapid increase of the viscoelastic loss modulus  $G''(\omega)$ , which in turn produces the strong IR absorption and broad Debye-like lineshape. The small convex-upward bump in  $\varepsilon'(\omega)$  near  $\omega_{\text{BP}}$  is accounted for by a shallow dip in the storage modulus  $G'(\omega)$  (Fig. S2), which lowers the transverse sound speed  $V_{\text{TA}}(\omega) = \sqrt{G'(\omega)/\rho}$ , and slightly flattens the  $\omega-k$  dispersion, yielding an excess VDOS in the BP region; accordingly, the  $\varepsilon'(\omega)$  bump reflects the BP-related excess. Within our isotropic three-dimensional formulation, Eq. (4), the transverse part of  $\varepsilon(\omega)$  is governed directly by the shear modulus  $G(\omega)$ , whereas the longitudinal part involves the longitudinal modulus  $M(\omega) = K + \frac{4}{3}G(\omega)$  and is therefore dominated by the nearly frequency-independent bulk modulus  $K$ . A decomposition of the modeled dielectric function into transverse and longitudinal contributions (Fig. S1) shows that, in the BP region, both  $\varepsilon'(\omega)$  and  $\varepsilon''(\omega)$  are almost entirely controlled by

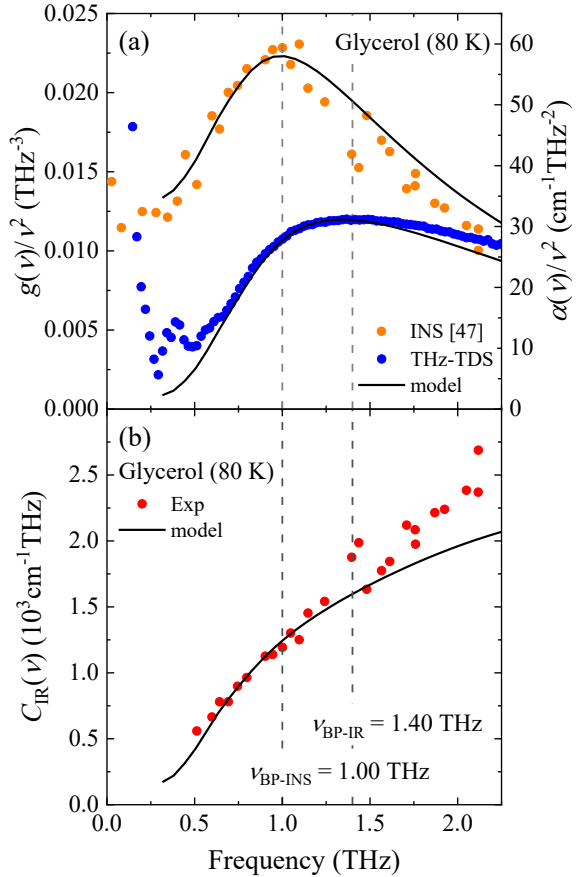


FIG. 2. Reduced spectra and IR light-vibration coupling. (a) Reduced absorption  $\alpha(\omega)/\omega^2$  (blue symbols) obtained from Fig. 1 via  $\alpha(\omega) = \omega\varepsilon''(\omega)/(cn'(\omega))$  (with  $c$  the speed of light and  $n'(\omega)$  the real part of the refractive index), together with the reduced VDOS  $g(\omega)/\omega^2$  (orange symbols) from independent inelastic neutron scattering (INS) [47]; solid lines are the model. (b)  $C_{\text{IR}}(\omega) = \alpha(\omega)/g(\omega)$ . The near-linear dependence around the BP is captured by the model, whereas the quadratic Taraskin form  $A + B\omega^2$  does not capture this trend. Vertical dashed lines mark the BP positions from IR and INS,  $\omega_{\text{BP-IR}}/2\pi \approx 1.40$  THz and  $\omega_{\text{BP-INS}}/2\pi \approx 1.00$  THz, respectively. Here  $\nu$  denotes the linear frequency,  $\nu = \omega/2\pi$ .

the transverse channel, with the longitudinal contribution remaining comparatively small over the whole band. Thus the BP-related THz dielectric response is controlled primarily by the frequency dependence of  $G(\omega)$  and the associated transverse-like vibrations.

Using the modeled dielectric function, we convert  $\varepsilon''(\omega)$  to the absorption coefficient  $\alpha(\omega)$  and, from the same effective modulus  $G(\omega)$ , obtain  $g(\omega)$ ; the reduced spectra  $\alpha(\omega)/\omega^2$  and  $g(\omega)/\omega^2$  are plotted in Fig. 2(a). We then form  $C_{\text{IR}}(\omega) = \alpha(\omega)/g(\omega)$  and compare with experiment. As shown in Fig. 2(b), the resulting  $C_{\text{IR}}(\omega)$  agrees with the data in the vicinity of the BP and captures the near-linear trend there, whereas the Taraskin form  $A + B\omega^2$  [35] cannot account for this trend.

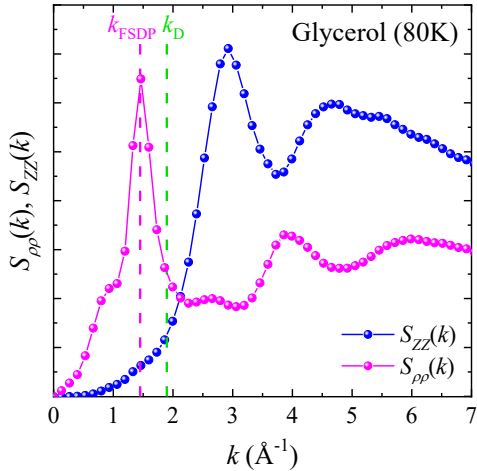


FIG. 3. Static charge and density correlations in glycerol glass (80 K). Shown are the charge-charge structure factor  $S_{ZZ}(k)$  (blue) and the mass-density static structure factor  $S_{pp}(k)$  (magenta) obtained from MD simulations. The FSDP and Debye wavenumbers ( $k_{\text{FSDP}}$ ,  $k_{\text{D}}$ ) are indicated.  $S_{pp}(k)$  exhibits a pronounced FSDP at  $k \sim 1.5 \text{ \AA}^{-1}$ , whereas  $S_{ZZ}(k)$  has no FSDP maximum; instead its first (lowest- $k$ ) maximum appears only at higher  $k$ , on the interatomic-spacing scale.

In Eq. (4) all microscopic information on the IR coupling is collected into the  $k$ -dependent oscillator strength  $\langle |\Delta q(k)|^2 \rangle_{\text{dis}}$ . Since the  $k$  integral is restricted to the acoustic window  $0 < k < k_{\text{D}}$ , we only require  $\Delta q(k)$  over this  $k$  range. Because the quantity entering Eq. (4) is the isotropic disorder-averaged oscillator strength  $\langle |\Delta q(k)|^2 \rangle_{\text{dis}}$ , which is expected to be a smooth (analytic) scalar function at  $k \rightarrow 0$ , we adopt the minimal quadratic form  $\Delta q(k) \approx q_0 + q_2 k^2$  and treat  $q_0$  and  $q_2$  as phenomenological parameters. Microscopically, however, the IR oscillator strength of each normal mode is determined by the mode-carried charge fluctuations, equivalently by the charge-charge dynamic structure factor  $S_{ZZ}(k, \omega)$  and its projection onto the eigenmodes [48, Chap. 10]. A fully microscopic determination of  $\Delta q(k)$  would thus require an explicit evaluation of  $S_{ZZ}(k, \omega)$ , which is beyond the scope of the present work. Here we use the static structure factor  $S_{ZZ}(k)$  from molecular dynamics (MD) [49] only as a qualitative diagnostic of medium-range charge correlations on the length scale associated with the first sharp diffraction peak (FSDP). For glycerol,  $S_{ZZ}(k)$  exhibits no maximum at the FSDP ( $k \sim 1.5 \text{ \AA}^{-1}$  [50]), and its lowest- $k$  maximum occurs at the interatomic-spacing scale (Fig. 3). Because the relevant  $k$  window ( $0 < k < k_{\text{D}}$ ) lies on the low- $k$  side of this maximum, the static  $S_{ZZ}(k)$  varies smoothly over the range contributing to Eq. (4). Accordingly, we do not introduce any explicit FSDP-like structure into the phenomenological  $\Delta q(k)$ .

For Fig. 1 we used  $\Delta q(k) = q_0 + q_2 k^2$  with a nearly

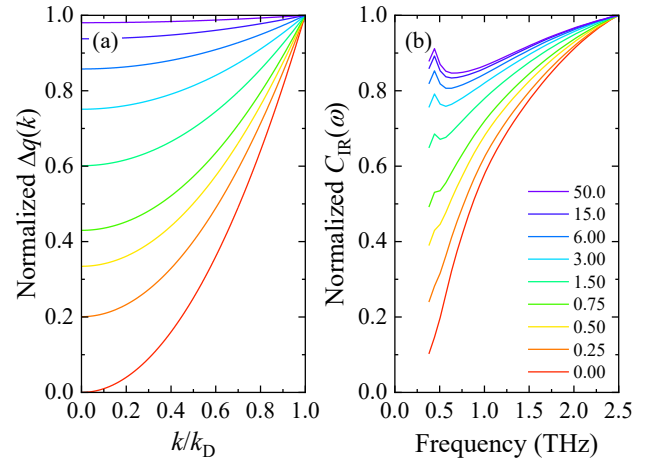


FIG. 4. Evolution with  $R = q_0/(q_2 k_{\text{D}}^2)$  in  $\Delta q(k) = q_0 + q_2 k^2$ : approaching the Taraskin-like regime. For each  $R$ ,  $q_0$  and  $q_2$  are rescaled to keep  $\int_0^{k_{\text{D}}} dk k^2 |\Delta q(k)|^2$  constant, isolating the effect of the  $k$ -independent term  $q_0$  (see Supplemental Material [38]). (a) Normalized  $\Delta q(k)$  (scaled to unity at  $k = k_{\text{D}}$ ) plotted as a function of  $k/k_{\text{D}}$  for several  $R$ . (b) Normalized  $C_{\text{IR}}(\omega)$  (scaled to unity at 2.5 THz) computed with the same  $G(\omega)$ . Increasing  $R$  strengthens the  $k$ -independent part of  $\Delta q(k)$  and drives  $C_{\text{IR}}(\omega)$  from a nearly linear form (small  $R$ ) toward the Taraskin-like behavior  $C_{\text{IR}}(\omega) \simeq A + B\omega^2$ .

vanishing constant term  $q_0$ . We fix  $q_0 = 0$  and select  $q_2$  by the parameter scan described above. With this choice the model yields a near-linear  $C_{\text{IR}}(\omega)$  in the vicinity of the BP. To clarify how this behavior evolves within our framework, we examine the dependence on the constant-term ratio  $R = q_0/(q_2 k_{\text{D}}^2)$ , which sets the balance between the  $k$ -independent ( $q_0$ ) and quadratic ( $q_2 k^2$ ) parts in  $\Delta q(k)$ . Increasing  $q_0$  enhances the  $k$ -independent weight of  $\langle |\Delta q(k)|^2 \rangle_{\text{dis}}$ —white in  $k$ —which, upon Fourier synthesis with random phases over  $k < k_{\text{D}}$ , corresponds to essentially white (spatially uncorrelated) charge fluctuations in real space. As the ratio  $R$  increases (Fig. 4(a)), the computed  $C_{\text{IR}}(\omega)$  evolves continuously toward a constant-term-dominated form (Fig. 4(b)). Within our framework the mechanism is direct: in the limit where the  $k$ -independent component dominates the  $\varepsilon(\omega)$  integral ( $\Delta q(k) \approx q_0$ ), the absorption  $\alpha(\omega)$  nearly follows the VDOS,  $\alpha(\omega) \propto g(\omega)/n'(\omega)$ ; hence  $C_{\text{IR}}(\omega)$  becomes only weakly frequency dependent.

Finally, we turn to the question of why Taraskin's model does not reproduce the nearly linear  $C_{\text{IR}}(\omega)$  observed near the BP. Taraskin's approach starts from a factorization ansatz  $\alpha(\omega) \approx C_{\text{IR}}(\omega)g(\omega)$  [35], motivated by the mode-resolved linear-response expression for crystals derived by Maradudin [34]. Microscopically, however, linear response gives  $\alpha(\omega) = \sum_{\kappa} C_{\kappa} \delta(\omega - \omega_{\kappa})$ , i.e., a sum over modes with mode-dependent couplings  $C_{\kappa}$ , not a product of a smooth coupling and the VDOS  $g(\omega) = \sum_{\kappa} \delta(\omega - \omega_{\kappa})$ . Identifying  $\alpha(\omega)$  with  $C_{\text{IR}}(\omega)g(\omega)$

amounts to a modeling assumption: it replaces the mode-resolved couplings  $C_\kappa$  by a single smooth function of frequency  $C_{\text{IR}}(\omega)$ . This limitation was emphasized early on for disordered solids, where absorption involves mode- (or subband-) resolved couplings that can vary strongly with frequency (see Galeener and Sen [51]). A related non-factorizable convolution form appears in low-frequency Raman scattering (Schmid and Schirmacher [52]). Under Taraskin's decomposition into uncorrelated and correlated charge components, this factorization yields the quadratic form  $C_{\text{IR}}(\omega) = A + B\omega^2$  used in their analysis. Within our framework, Eq. (4) can be interpreted as a continuum  $k$ -space coarse graining of Maradudin's mode-resolved linear-response formula [34], in which the discrete mode sum is replaced by an integral over  $k$  and the mode-dependent couplings are represented phenomenologically by an effective  $k$ -dependent oscillator strength  $\langle|\Delta q(k)|^2\rangle_{\text{dis}}$ . In this coarse-grained picture, the spectral factor is the viscoelastic Green's function of the acoustic branches,  $[-\omega^2 + \tilde{C}_\alpha(\omega)k^2]^{-1}$ , determined by the complex moduli  $G(\omega)$  and  $M(\omega)$ . A fully microscopic determination of these effective inputs is left for future work.

A continuum model based on IR-effective charge fluctuations  $\Delta q(k)$  and a frequency-dependent shear modulus  $G(\omega)$  reproduces the measured  $\varepsilon'(\omega)$ ,  $\varepsilon''(\omega)$ , and the near-linear  $C_{\text{IR}}(\omega)$  around the BP in glycerol glass. The single ratio  $R = q_0/(q_2 k_D^2)$  tunes the IR coupling from this linear regime toward the constant/quadratic-coupling behavior widely used to describe THz absorption in disordered materials,  $C_{\text{IR}}(\omega) = A + B\omega^2$ . With material-specific inputs, the framework is readily extendable to other glasses and provides a practical route to assess THz dielectric losses.

This work was supported by JSPS KAKENHI Grant Nos. 23H01139 and 23K25836 (to T.M.), 25H01519 and 22K03543 (to H.M.), and 24K08045 (to Y.F.); by the Asahi Glass Foundation (to T.M.); and by support from GIC & NGF (to T.M.).

## SUPPLEMENTAL MATERIAL

### CONTENT

*Organization of this Supplemental Material.*

Sections S1–S4 provide the derivation of the continuum formulation used in the main text.

Section S5 presents the transverse/longitudinal decomposition used for Fig. S1.

Section S6 describes the effective shear modulus  $G(\omega)$  used as a model input for glycerol.

Sections S7 and S8 document the molecular dynamics (MD) glass configuration and the evaluation of the static structure factors  $S_{\rho\rho}(k)$  and  $S_{ZZ}(k)$ .

Section S9 summarizes the parameter scan used to determine  $q_2$ .

Section S10 describes the rescaling procedure used for the  $R$ -scan in Fig. 4.

### S1. CONTINUUM EQUATION AND MODE DECOMPOSITION

We start from the elastodynamic equation used in the main text [Eq. (1)]:

$$\begin{aligned} -\rho\omega^2\mathbf{u}(\mathbf{r},\omega) = & \left(K + \frac{4}{3}G(\omega)\right)\nabla(\nabla \cdot \mathbf{u}(\mathbf{r},\omega)) - G(\omega)\nabla \times (\nabla \times \mathbf{u}(\mathbf{r},\omega)) \\ & + \Delta q(\mathbf{r})\mathbf{E}(\omega), \end{aligned} \quad (\text{S1})$$

with a spatially uniform terahertz (THz) field

$$\mathbf{E}(\omega) = E(\omega)\hat{\mathbf{e}}. \quad (\text{S2})$$

We introduce plane-wave expansions in a volume  $V$ ,

$$\begin{aligned} \mathbf{u}(\mathbf{r},\omega) &= \frac{1}{\sqrt{V}} \sum_{\mathbf{k}} \mathbf{u}(\mathbf{k},\omega) e^{i\mathbf{k}\cdot\mathbf{r}}, \\ \Delta q(\mathbf{r}) &= \frac{1}{\sqrt{V}} \sum_{\mathbf{k}} \Delta q(\mathbf{k}) e^{i\mathbf{k}\cdot\mathbf{r}}, \end{aligned} \quad (\text{S3})$$

where  $\Delta q(\mathbf{r})$  is real, so that

$$\Delta q(-\mathbf{k}) = \Delta q(\mathbf{k})^*. \quad (\text{S4})$$

For each wave vector  $\mathbf{k}$  we introduce three mutually orthonormal polarization vectors  $\hat{\mathbf{e}}_{\alpha}(\mathbf{k})$  ( $\alpha = L, T_1, T_2$ ):

$$\hat{\mathbf{e}}_L(\mathbf{k}) = \frac{\mathbf{k}}{k}, \quad \hat{\mathbf{e}}_{T_i}(\mathbf{k}) \cdot \mathbf{k} = 0, \quad \hat{\mathbf{e}}_{\alpha}(\mathbf{k}) \cdot \hat{\mathbf{e}}_{\alpha'}(\mathbf{k}) = \delta_{\alpha\alpha'}. \quad (\text{S5})$$

The displacement is decomposed as

$$\mathbf{u}(\mathbf{k},\omega) = \sum_{\alpha} u_{\alpha}(\mathbf{k},\omega) \hat{\mathbf{e}}_{\alpha}(\mathbf{k}), \quad (\text{S6})$$

and the real-field condition implies

$$u_{\alpha}(-\mathbf{k},\omega) = u_{\alpha}(\mathbf{k},\omega)^*. \quad (\text{S7})$$

Because the external THz field is spatially uniform, its component along branch  $\alpha$  is the scalar projection

$$E_{\alpha}(\omega) \equiv \hat{\mathbf{e}}_{\alpha}(\mathbf{k}) \cdot \mathbf{E}(\omega) = (\hat{\mathbf{e}} \cdot \hat{\mathbf{e}}_{\alpha}(\mathbf{k})) E(\omega). \quad (\text{S8})$$

Note that  $E_{\alpha}(\omega)$  depends on  $\mathbf{k}$  only through the polarization direction, whereas the field itself has no spatial modulation. Fourier transforming Eq. (S1), using Eq. (S6), and projecting onto  $\hat{\mathbf{e}}_{\alpha}(\mathbf{k})$  gives, after straightforward algebra,

$$(-\rho\omega^2 + C_{\alpha}(\omega)k^2)u_{\alpha}(\mathbf{k},\omega) = \Delta q(\mathbf{k})E_{\alpha}(\omega), \quad (\text{S9})$$

with

$$C_L(\omega) = M(\omega) = K + \frac{4}{3}G(\omega), \quad C_{T_1}(\omega) = C_{T_2}(\omega) = G(\omega). \quad (\text{S10})$$

Equation (S9) is the mode equation [Eq. (2) in the main text]. Solving Eq. (S9) for  $u_\alpha(\mathbf{k}, \omega)$  we obtain

$$u_\alpha(\mathbf{k}, \omega) = \frac{\Delta q(\mathbf{k})}{-\rho\omega^2 + C_\alpha(\omega)k^2} E_\alpha(\omega). \quad (\text{S11})$$

## S2. MACROSCOPIC POLARIZATION AND THE APPEARANCE OF $|\Delta q(\mathbf{k})|^2$

We are interested in the component of the macroscopic polarization parallel to the external field, defined as

$$P(\omega) = \frac{1}{V} \int d^3r \Delta q(\mathbf{r}) \hat{\mathbf{e}} \cdot \mathbf{u}(\mathbf{r}, \omega). \quad (\text{S12})$$

Inserting Eq. (S3) and the decomposition Eq. (S6) yields

$$\begin{aligned} P(\omega) &= \frac{1}{V} \int d^3r \left[ \frac{1}{\sqrt{V}} \sum_{\mathbf{k}} \Delta q(\mathbf{k}) e^{i\mathbf{k} \cdot \mathbf{r}} \right] \left[ \frac{1}{\sqrt{V}} \sum_{\mathbf{k}', \alpha} u_\alpha(\mathbf{k}', \omega) (\hat{\mathbf{e}} \cdot \hat{\mathbf{e}}_\alpha(\mathbf{k}')) e^{i\mathbf{k}' \cdot \mathbf{r}} \right] \\ &= \frac{1}{V} \sum_{\mathbf{k}, \mathbf{k}', \alpha} \Delta q(\mathbf{k}) u_\alpha(\mathbf{k}', \omega) (\hat{\mathbf{e}} \cdot \hat{\mathbf{e}}_\alpha(\mathbf{k}')) \int d^3r e^{i(\mathbf{k} + \mathbf{k}') \cdot \mathbf{r}}. \end{aligned} \quad (\text{S13})$$

The spatial integral produces a Kronecker delta (for a discrete  $\mathbf{k}$ -mesh),

$$\int d^3r e^{i(\mathbf{k} + \mathbf{k}') \cdot \mathbf{r}} = V \delta_{\mathbf{k}', -\mathbf{k}}, \quad (\text{S14})$$

so that

$$P(\omega) = \frac{1}{V} \sum_{\mathbf{k}, \alpha} \Delta q(\mathbf{k}) u_\alpha(-\mathbf{k}, \omega) (\hat{\mathbf{e}} \cdot \hat{\mathbf{e}}_\alpha(-\mathbf{k})). \quad (\text{S15})$$

Using Eqs. (S7) and (S5) ( $\hat{\mathbf{e}}_\alpha(-\mathbf{k}) = \hat{\mathbf{e}}_\alpha(\mathbf{k})$ ) and inserting Eq. (S11) gives

$$\begin{aligned} u_\alpha(-\mathbf{k}, \omega) &= u_\alpha(\mathbf{k}, \omega)^* = \frac{\Delta q(\mathbf{k})^*}{-\rho\omega^2 + C_\alpha(\omega)k^2} E_\alpha(\omega), \\ P(\omega) &= \frac{E(\omega)}{V} \sum_{\mathbf{k}, \alpha} \Delta q(\mathbf{k}) \Delta q(\mathbf{k})^* \frac{(\hat{\mathbf{e}} \cdot \hat{\mathbf{e}}_\alpha)^2}{-\rho\omega^2 + C_\alpha(\omega)k^2}. \end{aligned} \quad (\text{S16})$$

Thus the real-field condition directly leads to the combination

$$\Delta q(\mathbf{k}) \Delta q(\mathbf{k})^* = |\Delta q(\mathbf{k})|^2, \quad (\text{S17})$$

and we can rewrite Eq. (S16) as

$$P(\omega) = \frac{E(\omega)}{V} \sum_{\mathbf{k}, \alpha} \frac{|\Delta q(\mathbf{k})|^2}{-\rho\omega^2 + C_\alpha(\omega)k^2} (\hat{\mathbf{e}} \cdot \hat{\mathbf{e}}_\alpha)^2. \quad (\text{S18})$$

At this stage we have not yet made any statistical assumptions about  $\Delta q(\mathbf{r})$  or about the orientation of  $\mathbf{k}$  and  $\hat{\mathbf{e}}_\alpha$ .

## S3. DISORDER AVERAGE AND ORIENTATIONAL COUPLING FACTORS

We assume that the infrared (IR) effective charge fluctuations are statistically isotropic and homogeneous, with zero mean and short-range correlations. In  $\mathbf{k}$ -space this is expressed as

$$\overline{\Delta q(\mathbf{k})} = 0, \quad \overline{\Delta q(\mathbf{k}) \Delta q(\mathbf{k}')^*} = \delta_{\mathbf{k}, \mathbf{k}'} \langle |\Delta q(\mathbf{k})|^2 \rangle_{\text{dis}}, \quad (\text{S19})$$

where the overbar denotes a disorder average and  $\langle |\Delta q(k)|^2 \rangle_{\text{dis}}$  depends only on  $k = |\mathbf{k}|$ . Averaging Eq. (S18) over the disorder using Eq. (S19) gives

$$\overline{P(\omega)} = \frac{E(\omega)}{V} \sum_{\mathbf{k},\alpha} \frac{\langle |\Delta q(k)|^2 \rangle_{\text{dis}}}{-\rho\omega^2 + C_\alpha(\omega)k^2} (\hat{\mathbf{e}} \cdot \hat{\mathbf{e}}_\alpha)^2. \quad (\text{S20})$$

We now perform an orientational average over the relative angle between the external field direction  $\hat{\mathbf{e}}$  and the polarization basis  $\{\hat{\mathbf{e}}_\alpha(\mathbf{k})\}$ . We assume that the statistics of  $\Delta q(\mathbf{k})$  are independent of these orientations; hence the disorder and orientational averages factorize. We define the orientational coupling factor

$$\gamma_\alpha \equiv \langle (\hat{\mathbf{e}} \cdot \hat{\mathbf{e}}_\alpha)^2 \rangle_{\text{angles}}, \quad (\text{S21})$$

and replace  $(\hat{\mathbf{e}} \cdot \hat{\mathbf{e}}_\alpha)^2$  in Eq. (S20) by its angular average:

$$\overline{P(\omega)} = \frac{E(\omega)}{V} \sum_{\mathbf{k},\alpha} \frac{\langle |\Delta q(k)|^2 \rangle_{\text{dis}} \gamma_\alpha}{-\rho\omega^2 + C_\alpha(\omega)k^2}. \quad (\text{S22})$$

Using  $\varepsilon(\omega) = \varepsilon_\infty + \overline{P(\omega)}/[\varepsilon_0 E(\omega)]$ , Eq. (S22) yields the general discrete- $\mathbf{k}$  expression for the dielectric function:

$$\varepsilon(\omega) = \varepsilon_\infty + \frac{1}{\rho\varepsilon_0 V} \sum_{\mathbf{k},\alpha} \frac{\langle |\Delta q(k)|^2 \rangle_{\text{dis}} \gamma_\alpha}{-\omega^2 + \tilde{C}_\alpha(\omega)k^2}, \quad (\text{S23})$$

where  $\tilde{C}_\alpha(\omega) = C_\alpha(\omega)/\rho$ . Next we express the sum over  $\mathbf{k}$  in Eq. (S23) as an integral over an isotropic Debye sphere of radius  $k_D$ ,

$$\frac{1}{V} \sum_{\mathbf{k}} f(k) \longrightarrow \int_0^{k_D} f(k) \frac{3k^2}{k_D^3} dk. \quad (\text{S24})$$

This replacement follows the standard isotropic Debye prescription, whereby the discrete  $\mathbf{k}$  sum is approximated by a continuum integral over the isotropic Debye sphere  $0 < k < k_D$ , with  $k_D$  providing an interatomic-scale (short-wavelength) cutoff for the present continuum formulation. Using this replacement in Eq. (S23), we obtain the general branch-resolved expression for the dielectric function:

$$\varepsilon(\omega) = \varepsilon_\infty + \frac{1}{\rho\varepsilon_0} \sum_{\alpha} \int_0^{k_D} \frac{\langle |\Delta q(k)|^2 \rangle_{\text{dis}} \gamma_\alpha}{-\omega^2 + \tilde{C}_\alpha(\omega)k^2} \frac{3k^2}{k_D^3} dk. \quad (\text{S25})$$

This is Eq. (3) in the main text.

#### S4. ISOTROPIC LIMIT: $\gamma = 1/3$ AND THE FINAL EXPRESSION

In an isotropic three-dimensional elastic medium the three polarization vectors  $\{\hat{\mathbf{e}}_L, \hat{\mathbf{e}}_{T_1}, \hat{\mathbf{e}}_{T_2}\}$  form an orthonormal basis for any given  $\mathbf{k}$ . For a fixed  $\hat{\mathbf{e}}$  we always have

$$(\hat{\mathbf{e}} \cdot \hat{\mathbf{e}}_L)^2 + (\hat{\mathbf{e}} \cdot \hat{\mathbf{e}}_{T_1})^2 + (\hat{\mathbf{e}} \cdot \hat{\mathbf{e}}_{T_2})^2 = |\hat{\mathbf{e}}|^2 = 1. \quad (\text{S26})$$

Because the three directions are statistically equivalent, their orientational averages are identical:

$$\gamma_L = \gamma_{T_1} = \gamma_{T_2} \equiv \gamma. \quad (\text{S27})$$

Taking the orientational average of Eq. (S26) immediately gives

$$3\gamma = 1 \Rightarrow \gamma = \frac{1}{3}. \quad (\text{S28})$$

Substituting Eq. (S28) into Eq. (S25) and grouping the two degenerate transverse branches ( $C_{T_1} = C_{T_2} = G$ ) and the single longitudinal branch ( $C_L = M$ ), we obtain

$$\varepsilon(\omega) = \varepsilon_\infty + \frac{1}{\rho\varepsilon_0} \int_0^{k_D} \left[ \frac{2}{3} \frac{\langle |\Delta q(k)|^2 \rangle_{\text{dis}}}{-\omega^2 + \tilde{G}(\omega)k^2} + \frac{1}{3} \frac{\langle |\Delta q(k)|^2 \rangle_{\text{dis}}}{-\omega^2 + \tilde{M}(\omega)k^2} \right] \frac{3k^2}{k_D^3} dk, \quad (\text{S29})$$

where

$$\tilde{G}(\omega) = \frac{G(\omega)}{\rho}, \quad \tilde{M}(\omega) = \frac{M(\omega)}{\rho} = \frac{K + \frac{4}{3}G(\omega)}{\rho}. \quad (\text{S30})$$

Equation (S29) is identical to Eq. (4) of the main text, and is the working expression used in the analysis of the THz dielectric response.

## S5. BRANCH-RESOLVED POLARIZATIONS $P_T(\omega)$ AND $P_L(\omega)$ AND THE DIELECTRIC CONTRIBUTIONS

We define the branch-resolved contributions of the transverse and longitudinal acoustic branches to the field-parallel polarization  $P_T(\omega)$  and  $P_L(\omega)$ , as follows:

$$P_T(\omega) = \frac{E(\omega)}{V} \sum_{\mathbf{k}} \frac{|\Delta q(\mathbf{k})|^2}{-\rho\omega^2 + G(\omega)k^2} (\hat{\mathbf{e}} \cdot \hat{\mathbf{e}}_T)^2, \quad (\text{S31})$$

$$P_L(\omega) = \frac{E(\omega)}{V} \sum_{\mathbf{k}} \frac{|\Delta q(\mathbf{k})|^2}{-\rho\omega^2 + M(\omega)k^2} (\hat{\mathbf{e}} \cdot \hat{\mathbf{e}}_L)^2, \quad (\text{S32})$$

where in Eq. (S31)  $\hat{\mathbf{e}}_T$  represents one of the two transverse polarizations. In the isotropic limit each acoustic branch carries weight 1/3; combining the two degenerate transverse branches then gives

$$P(\omega) = \frac{2}{3}P_T(\omega) + \frac{1}{3}P_L(\omega), \quad (\text{S33})$$

and Eq. (S29) follows from  $\varepsilon(\omega) = \varepsilon_{\infty} + P(\omega)/[\varepsilon_0 E(\omega)]$  after applying the Debye-sphere replacement of the  $\mathbf{k}$  sum introduced above [Eq. (S24)]. Equation (S29) can therefore be viewed as a sum of transverse and longitudinal propagators. Using this branch-resolved decomposition, we define the corresponding contributions to the modeled dielectric function,  $\varepsilon_T(\omega)$  and  $\varepsilon_L(\omega)$ , which are shown in Fig. S1. Accordingly, we write

$$\varepsilon(\omega) = \varepsilon_{\infty} + \varepsilon_T(\omega) + \varepsilon_L(\omega), \quad (\text{S34})$$

with

$$\varepsilon_T(\omega) = \frac{1}{\rho\varepsilon_0} \int_0^{k_D} \left[ \frac{2}{3} \frac{\langle |\Delta q(k)|^2 \rangle_{\text{dis}}}{-\omega^2 + \tilde{G}(\omega)k^2} \right] \frac{3k^2}{k_D^3} dk, \quad (\text{S35})$$

$$\varepsilon_L(\omega) = \frac{1}{\rho\varepsilon_0} \int_0^{k_D} \left[ \frac{1}{3} \frac{\langle |\Delta q(k)|^2 \rangle_{\text{dis}}}{-\omega^2 + \tilde{M}(\omega)k^2} \right] \frac{3k^2}{k_D^3} dk. \quad (\text{S36})$$

Here  $\tilde{G}(\omega) = G(\omega)/\rho$  and  $\tilde{M}(\omega) = M(\omega)/\rho$  with  $M(\omega) = K + (4/3)G(\omega)$  as in Eq. (S30). Figure S1 summarizes the transverse and longitudinal dielectric contributions defined in Eqs. (S35) and (S36) by plotting their real and imaginary parts together with their sum,  $\varepsilon_T(\omega) + \varepsilon_L(\omega) = \varepsilon(\omega) - \varepsilon_{\infty}$ . Near the boson peak (BP) frequency  $\omega_{\text{BP}}/(2\pi) \simeq 1.0$  THz, both  $\varepsilon'(\omega)$  and  $\varepsilon''(\omega)$  are dominated by the transverse channel. This suppression of the longitudinal contribution follows directly from the structure of the longitudinal modulus,  $M(\omega) = K + (4/3)G(\omega)$ : in the THz range  $M(\omega)$  is largely controlled by the nearly frequency-independent bulk modulus  $K$ , whereas the strong frequency dependence of  $G(\omega)$  governs the transverse propagator and hence the observed BP-related THz dielectric response.

## S6. EFFECTIVE SHEAR MODULUS $G(\omega)$ USED FOR GLYCEROL

Our dielectric model requires the complex shear modulus  $G(\omega)$  as an input function. Importantly, the present formulation does not rely on a specific microscopic origin of the BP: any physically reasonable  $G(\omega)$  that reproduces the BP part of the reduced vibrational density of states (VDOS) is sufficient for the calculations discussed in the main text.

For glycerol, we obtain such an effective  $G(\omega)$  by applying a heterogeneous-elasticity-theory coherent-potential-approximation (HET-CPA) analysis of the experimental VDOS, following the procedure established in our previous work (see Ref. [44] for the full set of coherent potential approximation (CPA) equations, definitions of parameters, and fitting protocol). In brief, the HET-CPA analysis provides a self-consistent complex effective shear modulus  $G(\omega)$  whose parameters are chosen so that the calculated reduced VDOS matches the inelastic neutron scattering (INS) data of glycerol glass at 80 K [47] in the BP frequency range.

Figure S2(a) shows the resulting real and imaginary parts of  $G(\omega)$ , plotted in the normalized form  $\text{Re}[G(\omega)/G_0]$  and  $\text{Im}[G(\omega)/G_0]$ , where  $G_0$  is the geometric-mean shear modulus ( $G_0 = 5.43$  GPa). Using the same Green-function-based relation between  $G(\omega)$  and the VDOS as in Ref. [44], we compute the reduced VDOS  $g(\omega)/(A_D\omega^2)$  shown in Fig. S2(b), where  $A_D$  is the Debye level. The agreement with the INS spectrum demonstrates that the effective modulus used in the main-text dielectric calculations is consistent with the experimentally observed BP spectrum. Compared with Ref. [44], the CPA parameters controlling the coarse-graining cutoff and heterogeneity strength (denoted there by  $k_e$  and  $\sigma^2$ ) were adjusted slightly to reduce the dielectric misfit.

## S7. MOLECULAR DYNAMICS GLASS CONFIGURATION (GLYCEROL)

The atomistic glycerol glass structure shown in Fig. S3 was generated by classical molecular dynamics (MD) simulation using LAMMPS. The system contains  $N = 12096$  atoms, corresponding to  $N_{\text{mol}} = 864$  glycerol molecules in an all-atom representation (14 atoms per molecule), in a cubic periodic simulation cell of side length  $L = 47.16$  Å (mass density  $\rho = 1.26$  g cm<sup>-3</sup>).

The interatomic interactions were described by an all-atom AMBER-based glycerol force field following the reparameterized model of Blieck *et al.* [49], which is based on the AMBER glycerol model introduced by Chelli *et al.* [39, 40]. The specific parameter set employed here is summarized in Ref. [41]. Long-range electrostatics were treated using the particle-particle particle-mesh (PPPM) method in LAMMPS. Starting from an equilibrated liquid configuration at  $T = 350$  K, the system was cooled to  $T = 80$  K in the canonical (NVT) ensemble at fixed volume with a cooling rate of 0.4 K/ps to obtain a glassy state, subsequently equilibrated at 80 K. Figure S3 shows a representative snapshot from the equilibrated 80 K glass used for the structural analysis. The same 80 K configurations were used as input for the calculation of  $S_{\rho\rho}(k)$  and  $S_{ZZ}(k)$  described in the following subsection.

## S8. STATIC STRUCTURE FACTORS $S_{\rho\rho}(k)$ AND $S_{ZZ}(k)$

From the MD-generated glass configuration, we evaluate the mass-density static structure factor  $S_{\rho\rho}(k)$  and the (normalized) charge-charge structure factor  $S_{ZZ}(k)$ . We classify atomic sites into species (types)  $\alpha, \beta$ , with number fractions  $c_\alpha \equiv N_\alpha/N$  and total number density  $n \equiv N/V$ . From the partial pair correlation functions  $g_{\alpha\beta}(r)$  we define the total correlation functions:

$$h_{\alpha\beta}(r) \equiv g_{\alpha\beta}(r) - 1. \quad (\text{S37})$$

Assuming isotropy, we use the spherically averaged Fourier transform of  $h_{\alpha\beta}(r)$ . In practice the real-space integral is truncated at a maximum distance  $r_{\text{max}}$  (typically  $r_{\text{max}} = L/2$  for a cubic box of side length  $L$ ), and we apply the standard Lorch modification function  $f_L(r)$  to reduce termination artifacts [42]:

$$h_{\alpha\beta}(k) = 4\pi \int_0^{r_{\text{max}}} dr r^2 h_{\alpha\beta}(r) \frac{\sin(kr)}{kr} f_L(r),$$

$$f_L(r) = \frac{\sin(\pi r/r_{\text{max}})}{\pi r/r_{\text{max}}}. \quad (\text{S38})$$

The mass-density static structure factor is then evaluated in the Faber-Ziman form [43] as

$$S_{\rho\rho}(k) = 1 + \frac{n}{\bar{m}^2} \sum_{\alpha, \beta} c_\alpha c_\beta m_\alpha m_\beta h_{\alpha\beta}(k),$$

$$\bar{m} \equiv \sum_\gamma c_\gamma m_\gamma. \quad (\text{S39})$$

where  $m_\alpha$  is the atomic mass of species  $\alpha$  (note that  $n\bar{m} = \rho$ ).

For the charge-charge correlations, we use the same partial functions but weight them by the (dimensionless) partial charges  $z_\alpha$  (i.e., the atomic partial charge is  $ez_\alpha$ ). We follow the conventional multicomponent definition of the charge-charge structure factor [48, Chap. 10] and use the normalized form:

$$S_{ZZ}(k) = 1 + \frac{n}{\bar{z}^2} \sum_{\alpha, \beta} c_\alpha c_\beta z_\alpha z_\beta h_{\alpha\beta}(k),$$

$$\bar{z}^2 \equiv \sum_\gamma c_\gamma z_\gamma^2. \quad (\text{S40})$$

Charge neutrality implies  $\sum_\alpha c_\alpha z_\alpha = 0$ ; the above normalization corresponds to dividing the conventional  $S_{ZZ}(k)$  by  $\bar{z}^2$  and ensures  $S_{ZZ}(k) \rightarrow 1$  at large  $k$ .

### S9. PARAMETER SCAN FOR $q_2$

In the main text we use the long-wavelength form of the IR-effective charge fluctuation  $\Delta q(k) = q_0 + q_2 k^2$ . Because the calculated spectra are insensitive to  $q_0$  within the experimental uncertainty, we fix  $q_0 = 0$  (Table I) and determine  $q_2$  by a one-parameter scan. For each trial value of  $q_2$ , we compute the complex permittivity  $\varepsilon(\omega) = \varepsilon'(\omega) + i\varepsilon''(\omega)$  with all other model inputs fixed to the values listed in Table I. We then evaluate a scalar misfit (sum of squared residuals)

$$S(q_2) = \sum_{i=1}^N \left[ (\varepsilon'_{\text{calc}}(\omega_i; q_2) - \varepsilon'_{\text{exp}}(\omega_i))^2 + (\varepsilon''_{\text{calc}}(\omega_i; q_2) - \varepsilon''_{\text{exp}}(\omega_i))^2 \right], \quad (\text{S41})$$

where  $\{\omega_i\}$  are the experimental frequencies within the fitting window. We focus on the BP region (around  $\sim 1$  THz for glycerol) where the vibrational contribution is prominent. The scan was performed over  $q_2 = (1.25-1.90) \times 10^3 \text{ C cm}^{-3} \text{ \AA}^2$  with a step of  $0.005 \times 10^3 \text{ C cm}^{-3} \text{ \AA}^2$ , and Fig. S4 shows the normalized misfit  $S(q_2)/S_{\min}$ . A clear minimum is found at  $q_2 = 1.595 \times 10^3 \text{ C cm}^{-3} \text{ \AA}^2$  which is reported in Table I as  $q_2 = 1.6 \times 10^3 \text{ C cm}^{-3} \text{ \AA}^2$  (rounded). Repeating the scan for slightly shifted fitting windows within the experimental overlap changes the optimum by no more than one scan step (Fig. S4(b)).

### S10. RESCALING PROCEDURE FOR THE $R$ -SCAN IN FIG. 4

We parametrize the  $k$ -dependent effective charge fluctuation as

$$\Delta q(k) = q_0 + q_2 k^2, \quad (\text{S42})$$

and define the dimensionless ratio

$$R \equiv \frac{q_0}{q_2 k_D^2}, \quad (\text{S43})$$

which measures the relative weight of the  $k$ -independent component at the Debye wavenumber  $k_D$ . When scanning  $R$ , it is useful to isolate the effect of the shape of  $\Delta q(k)$  without allowing the overall fluctuation strength to grow artificially at large  $R$ . To this end, we rescale  $(q_0, q_2)$  for each  $R$  so that the Debye-sphere integrated strength is kept constant:

$$\int_0^{k_D} dk k^2 |\Delta q(k)|^2 = \text{const.} \quad (\text{S44})$$

Using  $\Delta q(k) = q_0 + q_2 k^2$ , the integral can be evaluated analytically as

$$\int_0^{k_D} dk k^2 (q_0 + q_2 k^2)^2 = q_0^2 \frac{k_D^3}{3} + 2q_0 q_2 \frac{k_D^5}{5} + q_2^2 \frac{k_D^7}{7}. \quad (\text{S45})$$

Substituting  $q_0 = R q_2 k_D^2$ , we obtain

$$\int_0^{k_D} dk k^2 |\Delta q(k)|^2 = q_2^2 k_D^7 J(R), \quad J(R) = \frac{R^2}{3} + \frac{2R}{5} + \frac{1}{7}. \quad (\text{S46})$$

We choose the constant to be equal to the  $R = 0$  value, for which  $q_0 = 0$  and  $q_2 = q_2^{(0)}$ . In the calculations for Fig. 4 we used  $k_D = 1.90 \text{ \AA}^{-1}$  and  $q_2^{(0)} = 1.595 \times 10^3 \text{ C cm}^{-3} \text{ \AA}^2$  (rounded to  $1.6 \times 10^3$  in Table I). This yields the rescaling formulas

$$q_2(R) = q_2^{(0)} \sqrt{\frac{(1/7)}{J(R)}}, \quad q_0(R) = R q_2(R) k_D^2. \quad (\text{S47})$$

This procedure keeps the overall fluctuation strength fixed while varying the relative weight of the  $k$ -independent component, thereby avoiding an artificial increase in the dielectric strength at large  $R$  and enabling a cleaner assessment of the  $R$ -dependence.

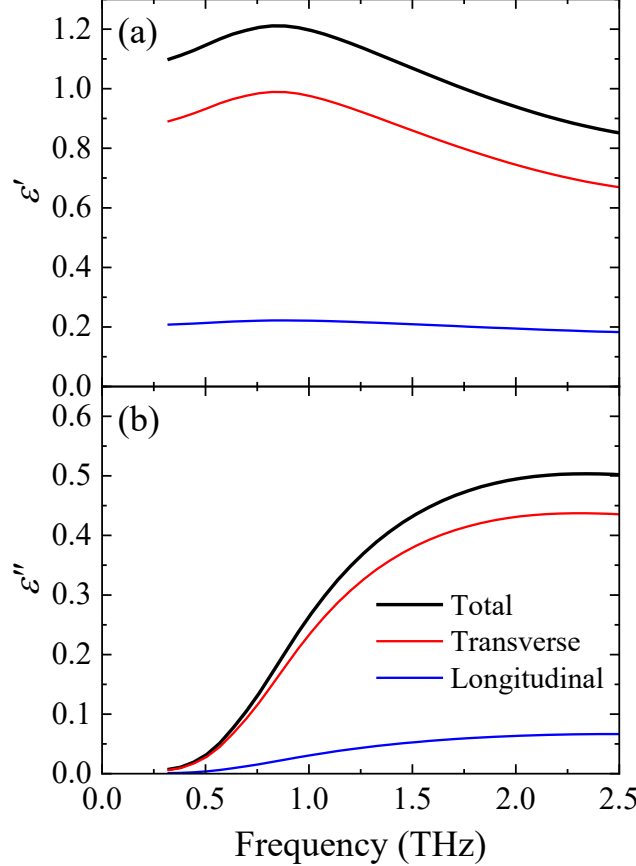


FIG. S1. Transverse and longitudinal contributions to the modeled complex dielectric function. (a) Real part and (b) imaginary part. Red: transverse contribution  $\epsilon_T(\omega)$ ; blue: longitudinal contribution  $\epsilon_L(\omega)$ ; black: total  $\epsilon_T(\omega) + \epsilon_L(\omega) = \epsilon(\omega) - \epsilon_\infty$ . The functions  $\epsilon_T(\omega)$  and  $\epsilon_L(\omega)$  are defined in Eqs. (S35) and (S36).

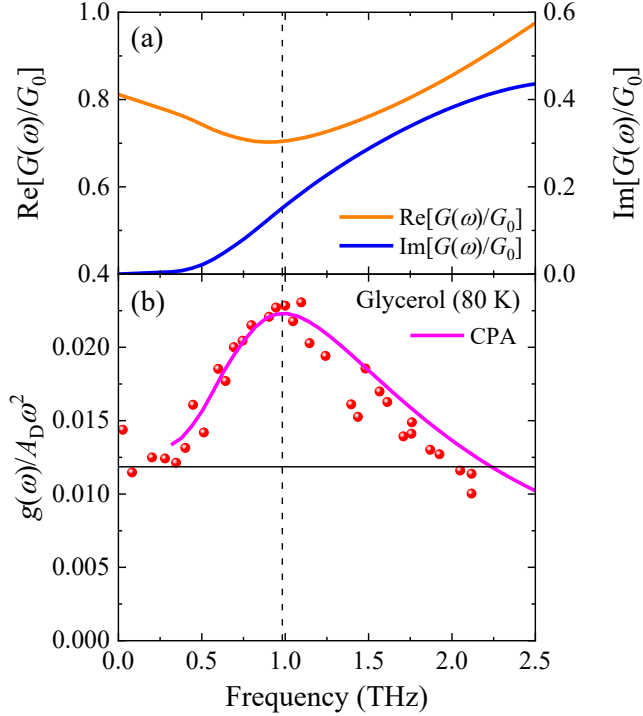


FIG. S2. (a) Real and imaginary parts of the effective shear modulus  $G(\omega)$  from the HET-CPA analysis, plotted as  $\text{Re}[G(\omega)/G_0]$  (orange) and  $\text{Im}[G(\omega)/G_0]$  (blue), with  $G_0 = 5.43$  GPa. (b) Reduced vibrational density of states  $g(\omega)/(A_D\omega^2)$  computed from  $G(\omega)$  (magenta line) compared with INS data [S2] (filled circles).

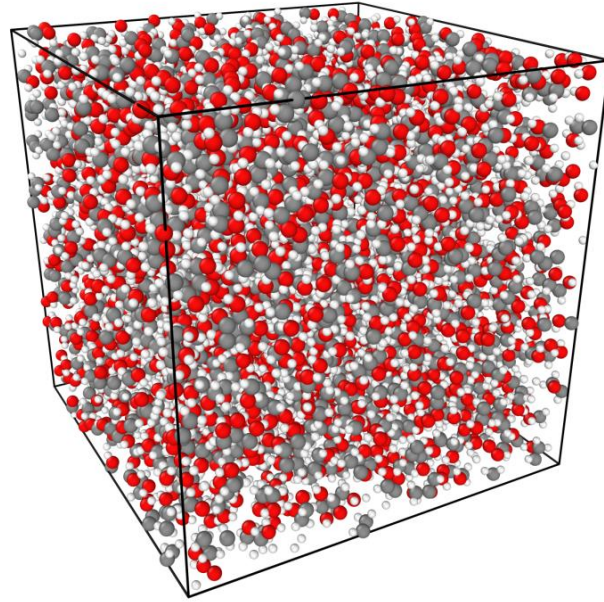


FIG. S3. Atomic configuration of glycerol glass at 80 K (MD). Representative MD snapshot of the 80 K glycerol glass used for the structure-factor analysis (basis for Fig. 3 in the main text).

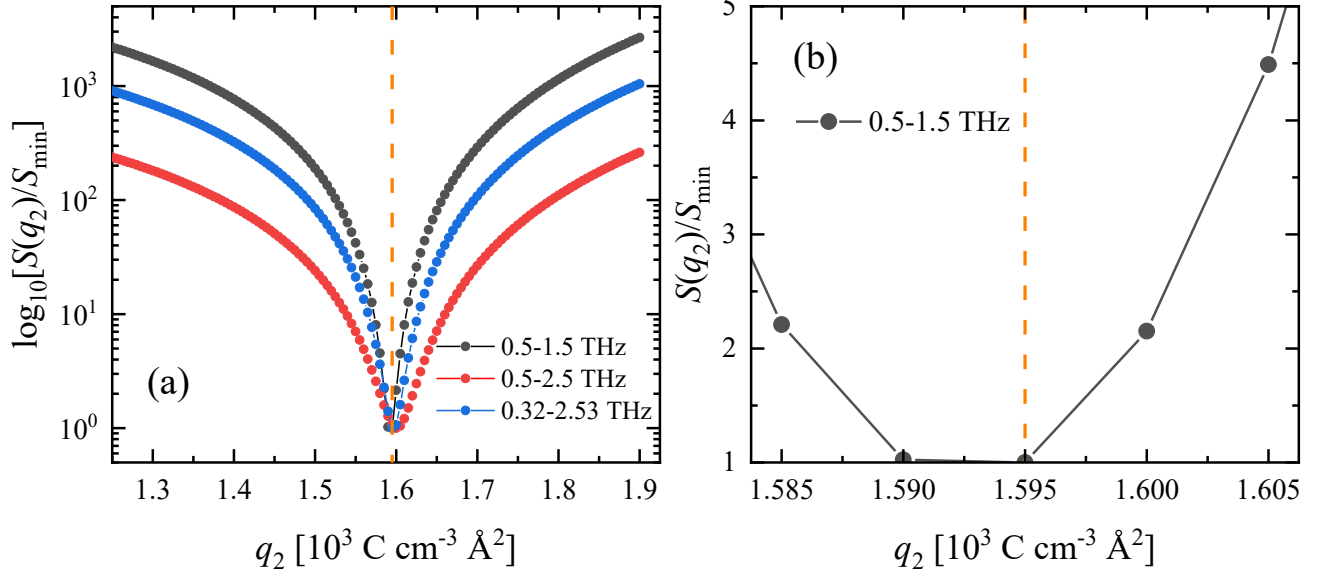


FIG. S4. Panel (a) shows  $\log_{10}[S(q_2)/S_{\min}]$  for three fitting windows within the experimental overlap, demonstrating that the minimum is robust. Panel (b) shows a zoom near the minimum for the main fitting window (0.5–1.5 THz). The dashed line marks the adopted value  $q_2 = 1.595 \times 10^3 \text{ C cm}^{-3} \text{ \AA}^2$ .

\* mori@ims.tsukuba.ac.jp

---

[1] T. Nakayama, *Rep. Prog. Phys.* **65**, 1195 (2002).

[2] M. A. Ramos, *Low-Temperature Thermal and Vibrational Properties of Disordered Solids* (World Scientific, London, 2022).

[3] R. C. Zeller and R. O. Pohl, *Phys. Rev. B* **4**, 2029 (1971).

[4] U. Buchenau, M. Prager, N. Nücker, A. J. Dianoux, N. Ahmad, and W. A. Phillips, *Phys. Rev. B* **34**, 5665 (1986).

[5] B. Rufflé, D. A. Parshin, E. Courtens, and R. Vacher, *Phys. Rev. Lett.* **100**, 015501 (2008).

[6] G. Baldi, V. M. Giordano, G. Monaco, and B. Ruta, *Phys. Rev. Lett.* **104**, 195501 (2010).

[7] A. I. Chumakov, G. Monaco, A. Monaco, W. A. Crichton, A. Bosak, R. Rüffer, A. Meyer, F. Kargl, L. Comez, D. Fioretto, H. Giefers, S. Roitsch, G. Wortmann, M. H. Manghnani, A. Hushur, Q. Williams, J. Balogh, K. Parliński, P. Jochym, and P. Piekarz, *Phys. Rev. Lett.* **106**, 225501 (2011).

[8] W. A. Phillips, *Amorphous Solids: Low-Temperature Properties* (Springer, Berlin, 1981).

[9] V. K. Malinovsky and A. P. Sokolov, *Solid State Commun.* **57**, 757 (1986).

[10] S. Kojima, *Phys. Rev. B* **47**, 2924 (1993).

[11] M. Kabeya, T. Mori, Y. Fujii, A. Koreeda, B. W. Lee, J.-H. Ko, and S. Kojima, *Phys. Rev. B* **94**, 224204 (2016).

[12] T. Mori, Y. Jiang, Y. Fujii, S. Kitani, H. Mizuno, A. Koreeda, L. Motoji, H. Tokoro, K. Shiraki, Y. Yamamoto, and S. Kojima, *Phys. Rev. E* **102**, 022502 (2020).

[13] H. Shintani and H. Tanaka, *Nat. Mater.* **7**, 870 (2008).

[14] A. Tanguy, B. Mantisi, and M. Tsamados, *Europhys. Lett.* **90**, 16004 (2010).

[15] S. Franz, G. Parisi, P. Urbani, and F. Zamponi, *Proc. Natl. Acad. Sci. U.S.A.* **112**, 14539 (2015).

[16] E. Lerner, G. Düring, and E. Bouchbinder, *Phys. Rev. Lett.* **117**, 035501 (2016).

[17] H. Mizuno, H. Shiba, and A. Ikeda, *Proc. Natl. Acad. Sci. U.S.A.* **114**, E9767 (2017).

[18] Y.-C. Hu and H. Tanaka, *Nat. Phys.* **18**, 669 (2022).

[19] E. Lerner and E. Bouchbinder, *J. Chem. Phys.* **158**, 194503 (2023).

[20] W. Schirmacher, *Europhys. Lett.* **73**, 892 (2006).

[21] W. Schirmacher, M. Paoluzzi, F. C. Mocanu, D. Khomenko, G. Szamel, F. Zamponi, and G. Ruocco, *Nat. Commun.* **15**, 3107 (2024).

[22] M. Wyart, *Europhys. Lett.* **89**, 64001 (2010).

[23] E. DeGiuli, A. Laversanne-Finot, G. Düring, E. Lerner, and M. Wyart, *Soft Matter* **10**, 5628 (2014).

[24] U. Buchenau, Y. M. Galperin, V. L. Gurevich, and H. R. Schober, *Phys. Rev. B* **43**, 5039 (1991).

[25] V. L. Gurevich, D. A. Parshin, and H. R. Schober, *Phys. Rev. B* **67**, 094203 (2003).

[26] C. Rainone, P. Urbani, F. Zamponi, E. Lerner, and E. Bouchbinder, *SciPost Phys. Core* **4**, 008 (2021).

[27] A. Moriel, E. Lerner, and E. Bouchbinder, *Phys. Rev. Research* **6**, 023053 (2024).

[28] R. T. Ako, A. Upadhyay, W. Withayachumnankul, M. Bhaskaran, and S. Sriram, *Adv. Opt. Mater.* **8**, 1900750 (2020).

[29] S. Havriliak and S. Negami, *Polymer* **8**, 161 (1967).

[30] L. Casella, M. Baggiooli, T. Mori, and A. Zaccione, *J. Chem. Phys.* **154**, 014501 (2021).

[31] E. A. DiMarzio and M. Bishop, *J. Chem. Phys.* **60**, 3802 (1974).

[32] K. Niss, B. Jakobsen, and N. B. Olsen, *J. Chem. Phys.* **123**, 234510 (2005).

[33] J. Kölbel, W. Schirmacher, E. Shalaev, and J. A. Zeitler, *Phys. Rev. B* **107**, 104203 (2023).

[34] A. A. Maradudin and R. F. Wallis, *Phys. Rev.* **123**, 777 (1961).

[35] S. N. Taraskin, S. I. Simdyankin, S. R. Elliott, J. R. Neilson, and T. Lo, *Phys. Rev. Lett.* **97**, 055504 (2006).

[36] Y. Hashimoto, T. Mori, and S. Kojima, *Mol. Cryst. Liq. Cryst.* **629**, 258 (2016).

[37] S. N. Taraskin, S. I. Simdyankin, and S. R. Elliott, *J. Phys.: Condens. Matter* **19**, 455216 (2007).

[38] See Supplemental Material for additional derivations and details of the HET-CPA analysis, the MD protocol, and the evaluation of the static structure factors, which includes Refs. [39–43].

[39] R. Chelli, P. Procacci, G. Cardini, R. G. Della Valle, and S. Califano, *Phys. Chem. Chem. Phys.* **1**, 871 (1999).

[40] R. Chelli, P. Procacci, G. Cardini, and S. Califano, *Phys. Chem. Chem. Phys.* **1**, 879 (1999).

[41] A. V. Egorov, A. P. Lyubartsev, and A. Laaksonen, *J. Phys. Chem. B* **115**, 14572 (2011).

[42] E. Lorch, *J. Phys. C: Solid State Phys.* **2**, 229 (1969).

[43] T. E. Faber and J. M. Ziman, *Philos. Mag.* **11**, 153 (1965).

[44] D. Kyotani, S. H. Oh, S. Kitani, Y. Fujii, H. Hijiya, H. Mizuno, S. Kohara, A. Koreeda, A. Masuno, H. Kawaji, S. Kojima, Y. Yamamoto, and T. Mori, *Sci. Rep.* **15**, 9617 (2025).

[45] Y. E. Ryabov, Y. Hayashi, A. Gutina, and Y. Feldman, *Phys. Rev. B* **67**, 132202 (2003).

[46] F. Scarponi, L. Comez, D. Fioretto, and L. Palmieri, *Phys. Rev. B* **70**, 054203 (2004).

[47] J. Wuttke, W. Petry, G. Coddens, and F. Fujara, *Phys. Rev. E* **52**, 4026 (1995).

[48] J.-P. Hansen and I. R. McDonald, *Theory of Simple Liquids*, 3rd ed. (Academic Press, Amsterdam, 2006).

[49] J. Blieck, F. Affouard, P. Bordat, A. Lerbret, and M. Descamps, *Chem. Phys.* **317**, 253 (2005).

[50] D. C. Champeney, R. N. Joarder, and J. C. Dore, *Mol. Phys.* **58**, 337 (1986).

[51] F. L. Galeener and P. N. Sen, *Phys. Rev. B* **17**, 1928 (1978).

[52] B. Schmid and W. Schirmacher, *Phys. Rev. Lett.* **100**, 137402 (2008).